International Journal of Intelligent Robotics and Applications
https://doi.org/10.1007/s41315-025-00421-x

REGULAR PAPER

Evaluating the interaction between human and paediatric robotic lower-limb exoskeleton: a model-based method

Mohammadhadi Sarajchi[1,2] · **Konstantinos Sirlantzis**[3]

Received: 14 October 2024 / Accepted: 6 January 2025

Abstract
Lower-limb exoskeletons (LLEs) have shown potential in improving motor function in patients for both clinical rehabilitation and daily life. Despite this, the development and control of pediatric exoskeletons remain notably underserved. This study focuses on a unique pediatric robotic lower limb exoskeleton (PRLLE), tailored particularly for children aged 8–12. Each leg of the robot has 5 Degrees of Freedom (DOFs)—three at the hip and one each at the knee and ankle. The interaction between the child user and the PRLLE is intricate, necessitating adherence to essential requirements of comfort, safety, and adaptability. Testing numerous prototype variations against diverse user profiles, particularly for children with neurological disorders where each child differs, is impractical. Model-based methods offer a virtual testbed that is useful in the design stage. This study uses MATLAB® to simulate and evaluate the interaction between users and PRLLE after deriving the nonlinear dynamic model of the PRLLE, which is simplified through multiple layers. To verify the accuracy of the derived dynamic model, a Computed Torque Control method is employed. The study provides detailed outcomes for children aged 8, 10, and 12 years, for passive and active users along with variations in PRLLE assistance levels. The study shows significant reductions in human joint torques, up to 56%, alongside substantial actuator powers, reaching up to 98W, for a 10-year-old child user. Furthermore, examining 8 and 12-year-old child users revealed variations in interaction forces, with changes up to 29.5%. Consequently, meticulous consideration of the human user's limitations is crucial during the PRLLE's design and conceptualization phases, particularly for PRLLEs.

Keywords Computed torque control · Dynamic modelling · Human–robot interaction · Lower-limb exoskeleton · Pediatric exoskeleton · Wearable robotics

1 Introduction

Motor dysfunction in children frequently arises from neurological or neuromuscular conditions such as cerebral palsy (CP), muscular dystrophy (MD), spinal muscular atrophy (SMA), and spinal cord injuries (SCI) (Alexander et al. 2015). CP, the most common mobility disorder in children, originates from brain injury or damage occurring before birth or in early childhood. Its incidence rate varies from 1 to almost 4 per 1000 live births (Rosenbaum et al. 2007; Aisen et al. 2011; Centers for Disease Control and Prevention 2022). MDs are chronic conditions that gradually impair muscles and limit activity. Among the nine primary types, Duchenne muscular dystrophy (DMD) is the most prevalent in childhood, affecting 1 in 5000 individuals (Duan et al. 2021). SMA, marked by spinal cord degeneration and muscle wasting, ranks as the second most common fatal autosomal recessive disorder following cystic fibrosis, with an incidence of 1 in 6000 to 1 in 10,000 live births (Swoboda 2010; Lunn and Wang 2008). In the pediatric demographic, SCIs are relatively uncommon, accounting for less than 4% of total annual SCI cases, but they have substantial psychological and physiological impacts (Parent et al. 2011).

These neurological conditions can significantly impact children's mobility, autonomy, and overall well-being

✉ Mohammadhadi Sarajchi
M.Sarajchi-2282@kent.ac.uk

Konstantinos Sirlantzis
konstantinos.sirlantzis@canterbury.ac.uk

[1] School of Engineering, University of Kent, Canterbury CT2 7NT, UK

[2] Bristol Robotics Laboratory, University of the West of England, Bristol BS16 1QY, UK

[3] School of Engineering, Technology and Design, Canterbury Christ Church University, Canterbury CT1 1QU, UK

Published online: 15 January 2025

(Bjornson et al. 2007; John et al. 2003). Furthermore, the impact on motor skill development is likely to become increasingly pronounced as children grow (Mutch et al. 1992). While there is no medical cure for these disorders, strong evidence suggests that powered assistance via wearable robotic LLEs can markedly enhance gait efficiency in those affected by these impairments (Orekhov et al. 2020; Bair May 2018; Sarajchi et al. 2021; World Health Organization 2006; Sarajchi and Sirlantzis 2023; Mohammadhadi 2024). Although some single-joint pediatric exoskeletons have been prototyped recently, the field still largely neglects the research and development on design, control, and analysis of full lower-limb structures with multiple actuated joints tailored explicitly for children (Sarajchi et al. 2021).

Designing effective exoskeletons is challenging due to the significant variations in physical dimensions and abilities among the target demographic, particularly for children with neurological disorders (Sarajchi et al. 2021; Rupal et al. 2017). Evaluating prototypes across a diverse target population can enhance exoskeleton design; however, this approach is costly, time-consuming, and can impose considerable strain on the participants. Model-based methods provide a viable alternative for testing exoskeleton designs and assessing human–exoskeleton interaction, offering a complementary solution to direct user testing (Manns et al. 2017; Vantilt et al. 2019). Researchers have employed multiple sensors on the thigh and shank to assess extreme forces during movement (Hsu et al. 2018). Additionally, mathematical models have been devised to predict lower limb contact forces during object lifting tasks (Chae et al. 2021). Nonetheless, the limited research on the physical human–exoskeleton interaction highlights a knowledge gap. This gap underscores the necessity to evaluate the contact forces exerted on humans by an PRLLE during walking, considering different assistance levels and variations in user size.

Dynamic modeling is crucial for robotic LLE design and control, enhancing stability, safety, and reducing human–robot interaction forces (Yan et al. 2019, 2024; Luo et al. 2024, 2022; Slucock 2022; Chen et al. 2023). A well-dynamically-tuned exoskeleton can assist children with gait challenges, enabling them to handle heavy loads and prolong demanding activities or conserve energy in specific tasks (Goo et al. 2022). Through dynamic modeling of the exoskeleton system, designers can analyze its behavior and refine its design (Goo et al. 2022). Furthermore, dynamic modeling aids designers in deriving the coupling dynamics between humans and exoskeletons, which is crucial for optimal user comfort and minimizing the forces (Hess-Coelho et al. 2022). Additionally, model-based control, a prevalent control strategy in LLEs, highly depends on the accuracy of the dynamic modeling of the device and the human–exoskeleton coupling dynamics (Yan et al. 2015). Despite these advantages, a reliable approach to derive and validate the dynamics of coupled human–exoskeleton systems in PRLLEs is highly demanded in the existing literature. This underscores an unexplored research gap in PRLLE technology, warranting deeper investigation.

Control strategies in wearable robotic LLEs remain an open challenge (Baud et al. 2021; Yu et al. 2023). Several studies have reviewed and compared diverse control strategies for LLEs (Yan et al. 2015; Baud et al. 2021; Tucker et al. 2015). Yan et al. (2015) classified various exoskeleton control strategies, with model-based control being the predominant choice. While model-based control requires an accurate dynamic model of the LLE, it offers advantages over model-free controllers. Model-based control strategies rely on mathematical models of the system to design controllers that ensure robust tracking performance (Saeed et al. 2022). Moreover, a model-based control method can utilize a dynamic model of the exoskeleton to compensate for its own dynamics. After this compensation of the exoskeleton dynamics, the exoskeleton can provide a desired assistance to the user (Vantilt et al. 2019). Model-based control strategies can also compensate for gravity, determine the assistance, and even incorporate balance criteria (Vantilt et al. 2019). In contrast, model-free control strategies do not require an exact mathematical model of the system, but instead approximate the system function using techniques such as radial basis function neural networks (RBFNNs) (Saeed et al. 2022). While this approach can achieve desired results with minimum tracking error, it may not be as precise as a model-based control strategy (Saeed et al. 2022).

This paper addresses a research gap in the PRLLE literature, focusing on the physical human–robot interaction while the child user engages in an assisted gait trajectory. Within this framework, the following contributions of a pediatric hip–knee–ankle–foot exoskeleton with five joints per leg are derived from this research: (i) forward kinematic analysis of the PRLLE; (ii) comprehensive dynamic modelling of the coupled human–PRLLE system; (iv) a model validation approach using the Simulink® and Simscape™ computational environments; (v) simulation modelling the PRLLE's capabilities across varying body proportions, specifically for child users aged 8, 10, and 12 years, and quantifying levels of assistance at 30% and 60%; (vi) computing and analyzing the interaction forces and torques between the child and the PRLLE to evaluate wearability and user comfort.

2 Exoskeleton and mathematical model

This section analyzes a PRLLE designed to support children's lower limb motion and promote stable gait. This prototype is size-adjustable to accommodate a wide range of children ages 8–12, based on an extensive anthropometric study, detailed in Table 1. This assistive device features 5

Table 1 Average body dimensions of children at the 50th percentile, complemented by the maximum and minimum dimensions of the Prlle (Whitley et al. 2009; Fryar et al. 2012)

Type	Children		PRLLE	
Gender	Girls	Boys	–	–
Age (years)	8	12	min	MAX
H (cm)	123.6 ± 5.6	141 ± 6.9	115	148
LL (cm)	71.9 ± 3.9	84.5 ± 4.7	65	91
ULL (cm)	31.9 ± 1.8	39.1 ± 2.1	29	42
LLL (cm)	40.0 ± 2.1	45.4 ± 2.6	36	49
FL (cm)	18.6 ± 1.2	21.4 ± 1.2	23.5	23.5

H Height, *LL* Leg Length, *FL* Foot Length, *ULL* Upper Leg Length, *LLL* Lower Leg Length

DOFs for each leg: three situated at the hip and one respectively at the knee and ankle. The PRLLE is outfitted with actuators powered by Brushless DC Maxon motors paired with Harmonic Drive gears. The communication protocol utilizes EtherCAT, with a Speedgoat Unit real-time target machine functioning as the EtherCAT Master. Each actuator is supported by an EPOS4 driver, serving as the EtherCAT Slave. Additionally, IMUs and ground reaction force sensors are integrated into the PRLLE's feet. The detailed design description of the PRLLE can be found in Sarajchi and Sirlantzis (2023).

Figure 1 depicts both the physical and virtual prototypes of the assistive device. Additionally, the cartesian coordinate frames associated with the right leg of the PRLLE, along with the joint configuration, are illustrated in this figure. Forward kinematic analysis is fundamental for deriving the PRLLE's dynamic model; hence, this section provides a detailed examination of the kinematic model. As the physical prototype is unpowered in this study, the virtual prototype will be employed for system modeling and controller design.

2.1 Forward kinematic analysis

Forward kinematics utilizes segment lengths and joint angles to determine the orientation and position of the end-effector, for example, the forefoot, with respect to a reference origin. This procedure translates the PRLLE joints' motion into foot movement, facilitating accurate control and analysis of gait patterns (Hasnain Baluch et al. 2012; Spong et al. 2006). Forward kinematic analysis gives designers insight into the PRLLE's motion and aids in using transformation matrices for formulating a distinct dynamic model, leading to a model-based controller for the PRLLE (Spong et al. 2006; Andrade et al. 2019).

Figure 1D shows that each leg is independent, allowing the PRLLE's forward kinematics to be decomposed into two kinematic chains with 5 DOF each. The Denavit–Hartenberg (D–H) convention is the most prevalent method for deriving forward kinematics (Denavit and Hartenberg 1955). In Table 2, the D–H parameters for each leg are detailed: θ_i and d_i correspond to the angle and offset of the

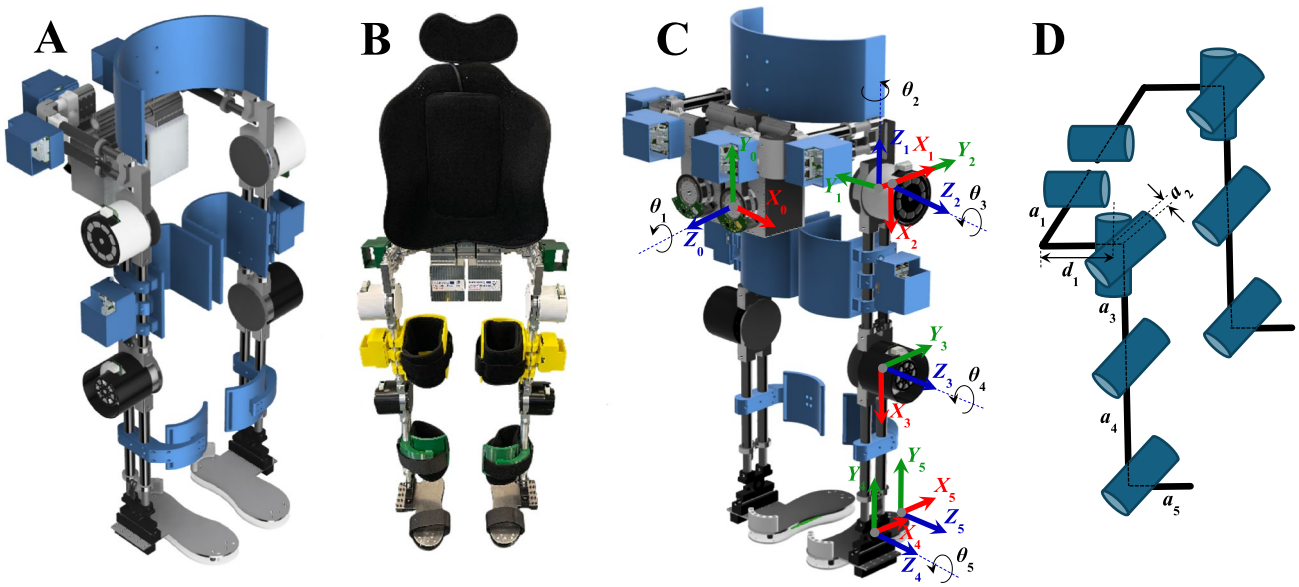

Fig. 1 Paediatric Lower Limb Exoskeleton structure. **A** Front view of the virtual prototype; **B** Physical PRLLE; **C** Back view of the virtual prototype with assigned Cartesian coordinate frames to the right leg; **D** Joint configuration of the PRLLE

Table 2 D-H Parameters for Each Leg of the PRLLE

Link	Right leg				Left leg			
	θ_i	d_i	a_i	α_i	θ_i	d_i	a_i	α_i
1	θ_1	d_1	a_1	$-\pi/2$	$\theta_1+\pi$	d_1	a_1	$\pi/2$
2	$\theta_2+\pi/2$	0	a_2	$\pi/2$	$\theta_2-\pi/2$	0	a_2	$-\pi/2$
3	$\theta_3-\pi/2$	0	a_3	0	$\theta_3+\pi/2$	0	a_3	0
4	θ_4	0	a_4	0	θ_4	0	a_4	0
5	$\theta_5+\pi/2$	0	a_5	0	$\theta_5-\pi/2$	0	a_5	0

*i*th joint, respectively, while a_i and α_i represents the length and twist of the *i*th link. Let's use the following abbreviations: S_1 for $\sin(\theta_1)$, C_1 for $\cos(\theta_1)$, S_{34} for $\sin(\theta_3+\theta_4)$, S_{345} for $\sin(\theta_3+\theta_4+\theta_5)$, C_{34} for $\cos(\theta_3+\theta_4)$, and C_{345} for $\cos(\theta_3+\theta_4+\theta_5)$. The homogeneous transformation matrices corresponding to the right leg of the PRLLE are as follows:

$$T_0^1=\begin{bmatrix} C_1 & 0 & -S_1 & a_1C_1 \\ S_1 & 0 & C_1 & a_1S_1 \\ 0 & -1 & 0 & d_1 \\ 0 & 0 & 0 & 1 \end{bmatrix}, T_1^2=\begin{bmatrix} -S_2 & 0 & C_2 & -a_2S_2 \\ C_2 & 0 & S_2 & a_2C_2 \\ 0 & 1 & 0 & 0 \\ 0 & 0 & 0 & 1 \end{bmatrix}$$
$$T_2^3=\begin{bmatrix} S_3 & C_3 & 0 & a_3S_3 \\ -C_3 & S_3 & 0 & -a_3C_3 \\ 0 & 0 & 1 & 0 \\ 0 & 0 & 0 & 1 \end{bmatrix}, T_3^4=\begin{bmatrix} C_4 & -S_4 & 0 & a_4C_4 \\ S_4 & C_4 & 0 & a_4S_4 \\ 0 & 0 & 1 & 0 \\ 0 & 0 & 0 & 1 \end{bmatrix} \quad (1)$$
$$T_4^5=\begin{bmatrix} -S_5 & -C_5 & 0 & -a_5S_5 \\ C_5 & -S_5 & 0 & a_5C_5 \\ 0 & 0 & 1 & 0 \\ 0 & 0 & 0 & 1 \end{bmatrix}$$

Using the derived homogeneous transformation matrices in Eq. (1), the forward kinematics of the PRLLE's right leg is formulated as:

$$T_0^5=T_0^1T_1^2T_2^3T_3^4T_4^5=\begin{bmatrix} -S_1S_{345}-C_1S_2C_{345} & C_1S_2S_{345}-S_1C_{345} & C_1C_2 & P_x \\ C_1S_{345}-S_1S_2C_{345} & C_1C_{345}+S_1S_2S_{345} & S_1C_2 & P_y \\ -C_2C_{345} & C_2S_{345} & -S_2 & P_z \\ 0 & 0 & 0 & 1 \end{bmatrix} \quad (2)$$

where P_x, P_y, and P_z are the Cartesian coordinates of the PRLLE's right foot end-effector relative to the X_0, Y_0, and Z_0 axes, respectively. These positions are given by:

$$P_x=a_1C_1+S_1\left(a_3C_3+a_4C_{34}-a_5S_{345}\right)-C_1S_2(a_2+a_3S_3+a_4S_{34}+a_5C_{345}) \quad (3)$$

$$P_y=a_1S_1+C_1\left(a_3C_3+a_4C_{34}-a_5S_{345}\right)-S_1S_2(a_2+a_3S_3+a_4S_{34}+a_5C_{345}) \quad (4)$$

$$P_z=d_1-C_2(a_2+a_3S_3+a_4S_{34}+a_5C_{345}) \quad (5)$$

This section detailed the forward kinematics for the right leg. The left leg's kinematics can be similarly derived using parameters from Table 2.

2.2 Dynamic modelling

In this section, the dynamic model of the coupled human–PRLLE system is derived using the forward kinematic analysis outlined earlier. This deepens comprehension of the human–PRLLE system's intricate behavior and facilitates the development of a model-based control algorithm. The dynamic model of a coupled human–PRLLE system based on the Euler–Lagrange formulation is delineated as follows:

$$M(q)\ddot{q}+C(q,\dot{q})\dot{q}+G(q)=\tau \quad (6)$$

where $M(q)$, $C(q,q)$, and $G(q)$ represent the inertia matrix, the Coriolis and centripetal matrix, and the gravity vector, respectively; furthermore, q denotes the vector of the PRLLE's joint positions, and τ signifies the torque generated by PRLLE motors and human user's joints. In this study, the human user's engagement with the PRLLE system is categorized into two modes: passive and active. In the active mode, the user actively contributes torque to the system. The parameters for each leg of the PRLLE with 5 DOFs can be derived as follows (Spong et al. Dec. 2006):

$$M(q)=\sum_{i=1}^{5}\left(m_iJ_{vi}^TJ_{vi}+J_{wi}^TR_0^iI_{ci}R_0^{i\,T}J_{wi}\right) \quad (7)$$

$$C(q,\dot{q}) = \frac{1}{2}\sum_{i=1}^{5}\left(\frac{\partial M_{kj}}{\partial q_i} + \frac{\partial M_{ik}}{\partial q_j} - \frac{\partial M_{ij}}{\partial q_k}\right)\dot{q}_i \tag{8}$$

$$G(q) = \begin{pmatrix} \frac{\partial P}{\partial q_1} & \cdots & \frac{\partial P}{\partial q_5} \end{pmatrix}^T \tag{9}$$

In this context, m_i denotes mass, J_{vi} and J_{wi} signify linear and angular Jacobians, respectively, R_i is the rotational matrix for the i-th link in the coupled human–PRLLE system, and P encapsulates the potential energy. The extension of these equations for the right leg of the coupled human–PRLLE system is detailed in *Appendix A*. Given the identical DOF and comparable mechanical configuration, the dynamic model for the left leg can be derived using a similar approach. Equation (6) outlines the inverse dynamics of the coupled human–exoskeleton system, while its forward dynamic equation, valuable for simulation modeling, is presented below:

$$\ddot{q} = M(q)^{-1}(\tau - C(q,\dot{q})\dot{q} - G(q)) \tag{10}$$

The forward dynamics model is directly implemented in MATLAB Simulink® via a MATLAB Function to simulate the coupled human–exoskeleton system. This methodology allows dynamic system simulation under various conditions, streamlines its theoretical analysis, and facilitates model-based controller design.

2.3 Controller design

2.3.1 Passive human user

Considering the availability of an accurate dynamic model for the coupled human–PRLLE system with passive human user, Computed Torque Control (CTC) appears to be an apt choice for precise trajectory tracking, as described below (Spong et al. 2006; Han et al. 2020) (Fig. 2):

$$\widetilde{M}(q)(\ddot{q}_d + K_d(\dot{q}_d - \dot{q}) + K_p(q_d - q)) + \widetilde{C}(q,\dot{q}) + \widetilde{G}(q) = \tau \tag{11}$$

In the given model, $\widetilde{M}(q)$ represents the estimated mass matrix, $\widetilde{C}(q,\dot{q})$ denotes the estimated Coriolis and centripetal matrix, and $\widetilde{G}(q)$ is the estimated gravity vector. Additionally, q_d is the vector specifying the PRLLE's desired joint positions. The matrices K_p and K_d are diagonal with positive scalar entries. CTC typically involves two main components: a proportional-derivative (PD) feedback control term and a feedforward term based on the calculated inverse dynamics torques. The PD feedback control term helps in minimizing the tracking error between the current state of the PRLLE and the desired trajectory. The feedforward term uses the calculated inverse dynamics torques to compensate for the robot's dynamics (Spong et al. 2006; Lynch and Park 2017). Taking into account Eqs. (6) and (11), and assuming an accurate estimated dynamic model where $(\widetilde{M}(q) = M(q))$, $(\widetilde{C}(q,\dot{q}) = C(q,\dot{q}))$, and $(\widetilde{G}(q) = G(q))$, we obtain:

$$\ddot{q} = \ddot{q}_d + K_d(\dot{q}_d - \dot{q}) + K_p(q_d - q) \tag{12}$$

Define the angular error vector and its derivatives as follows:

$$q_e = q_d - q; \dot{q}_e = \dot{q}_d - \dot{q}; \ddot{q}_e = \ddot{q}_d - \ddot{q} \tag{13}$$

Then, (12) can be reformulated as follows:

$$\ddot{q}_e + K_d\dot{q}_e + K_p q_e = 0 \tag{14}$$

For PRLLE systems, a smooth and soft response with no overshoot is desired (Layne et al. 2022), necessitating a critically damped response where the damping ratio is unity. The condition for critical damping is expressed as:

$$K_d = 2\sqrt{K_p} \tag{15}$$

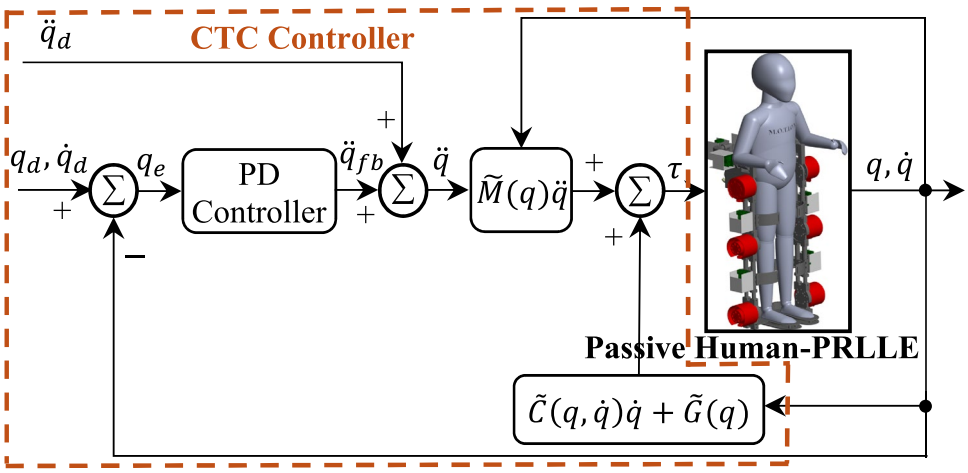

Fig. 2 Diagram of Computed Torque Control with Passive Human User (PRLLE provides 100% of the torques): The feedforward acceleration $\ddot{q}_d$ is combined with the feedback acceleration $\ddot{q}_{fb}$ from the PD controller to produce the commanded acceleration $\ddot{q}$

2.3.2 Active human user

The PRLLE's actuator torques were regulated to supply a variable proportion of the total torque needed to follow a prescribed gait trajectory. The total torque, τ_{CTC}, was calculated using the CTC controller shown in Fig. 2 for the human–PRLLE system with a passive human user, where the PRLLE supplied 100% of the torques necessary for the prescribed gait trajectory. In the forward dynamics simulations, a scalar variable C is introduced to enable the PRLLE assist range from 0 to 100%. For the dynamics simulations, the PRLLE reference torque was computed as $\tau_{ref} = C\tau_{CTC}$. Each leg was equipped with four PID controllers, one per actuator, designed to minimize the error between τ_{ref} and τ_{exo}, with τ_{exo} being the PRLLE torques calculated in the dynamics simulation. Controller parameters were optimized using MATLAB's control tuner toolbox for a step response with minimal overshoot and rapid actuator rise time. The block diagram of the control system for an active human user is presented in Fig. 3.

3 Human–PRLLE modelling and simulation

Using CAD Software, the human and LLE were modelled as distinct chains of rigid bodies and connected at contact points. Subsequently, the coupled human–PRLLE system was imported into MATLAB Simulink-Simscape for advanced simulation analysis. The model repository, including simulation files and associated results data, is available under an open-source license, as detailed in *Appendix B*.

3.1 CAD modelling

In this study, SolidWorks™ Student Edition (2021–2022) (Dassault Systèmes, France) was utilized as CAD software for the mechanical design and modeling of the PRLLE. Each leg of the PRLLE is equipped with 5-DOF revolute joints: 3 for the hip, 1 for the knee, and 1 for the ankle. Motors, gearboxes, sensors, and drivers are imported as STEP files from the affiliated company's website into the CAD model. Moreover, auxiliary components such as motor/driver housings, tubes, clamps, etc., are meticulously designed using SolidWorks™. The mass properties of the PRLLE were calculated using geometric meshes, with the assumption that all links are constructed from aluminum alloy and braces are made from polyethylene foam. The total mass of the PRLLE, not including human weight, was determined to be 16.66 kg. The dimensions of the PRLLE are delineated in Fig. 4A, featuring size-adjustable thigh and shank components. The thigh link spans a length of 290–420 mm, while the shank link ranges from 360 to 490 mm. The PRLLE was specifically calibrated to accommodate a 10-year-old male as a "nominal" human model (Whitley et al. 2009; Fryar et al. 2012). The length and mass of the right leg of the PRLLE are detailed in Table 3. The left leg mirrors the right and possesses identical values.

Moreover, a Q-6 dummy demo model, sourced from reference (3D Human Model xxxx), was imported into SolidWorks™ to represent the human user. The anthropometric data for the nominal human user corresponds to an 10-year-old male with a height of 1.33 m and a weight of 38.0 kg (Whitley et al. 2009; Fryar et al. 2012) (Fig. 4A). Similarly, two human models, smaller and larger than the nominal, were developed to represent an 8-year-old female and a 12-year-old male, respectively (Whitley et al. 2009; Fryar et al. 2012). Similar to the PRLLE, each human leg has a 5-DOF revolute joint configuration: three at the hip, one at the knee, and one at the ankle, ensuring full compatibility with the PRLLE's mechanical structure. For this study, all upper limb segments were kinematically fixed. The human was connected to the PRLLE via braces on the thigh, shank, and foot segments as weld joints to create a virtual prototype of the coupled human–PRLLE system (Fig. 4A). For dynamic analysis and controller implementation of the coupled human–PRLLE system (virtual prototype), the model was exported from SolidWorks™ and imported into MATLAB Simscape™ and named "Detailed Model".

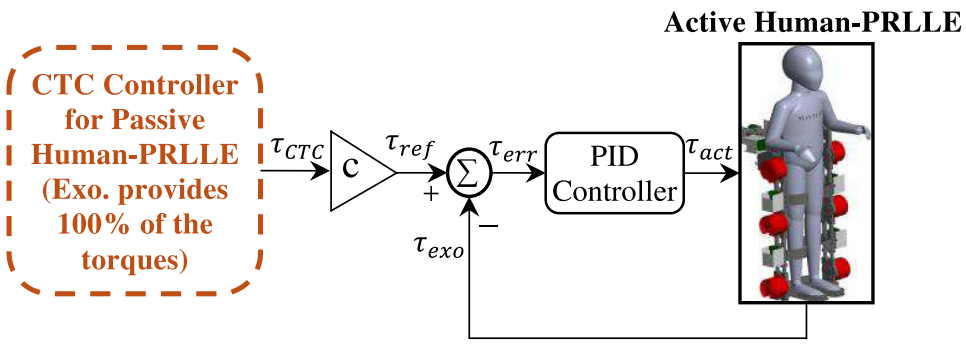

Fig. 3 Schematic illustrates the control system of the PRLLE with an active human user. τ_{CTC} represents the torques necessary for the PRLLE to perform the predefined gait trajectory with a completely passive human user. τ_{ref} signifies the portion of τ_{CTC} used as reference torques in the PID controller. τ_{exo} denotes the torque generated by the PRLLE

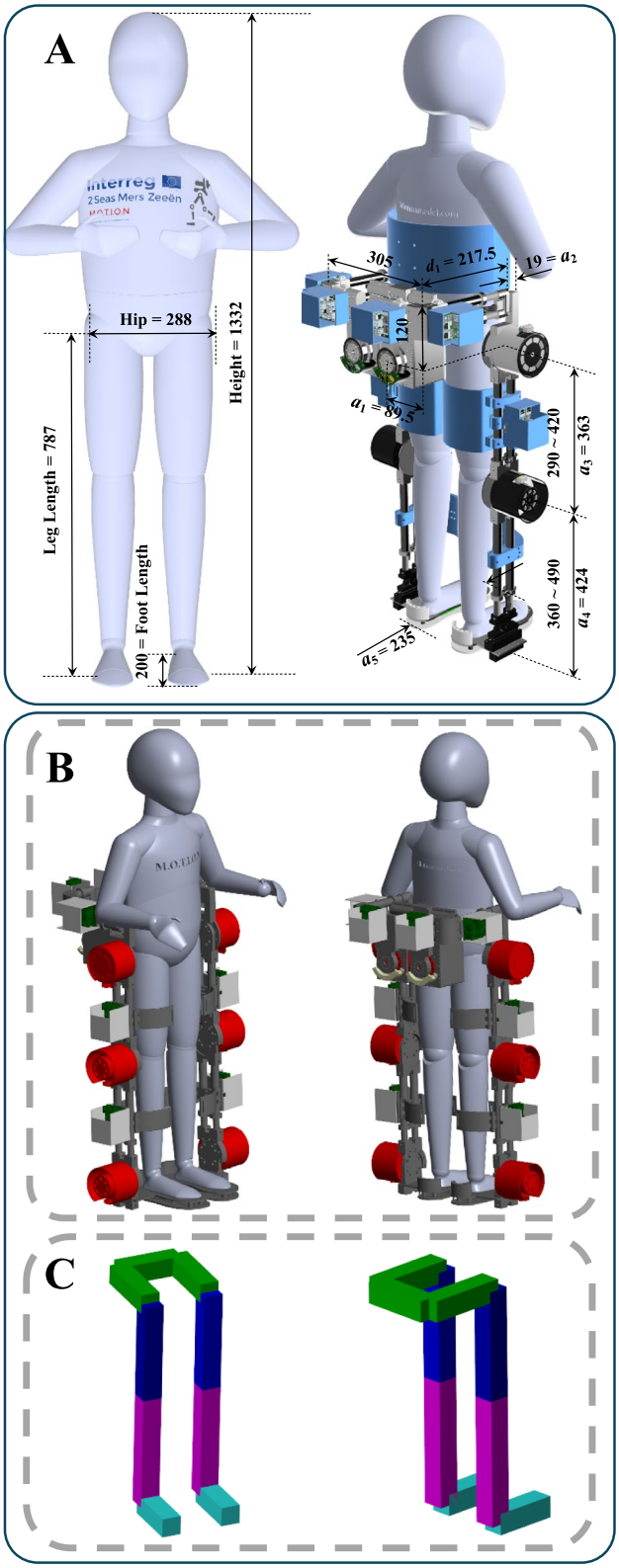

Fig. 4 Human and PRLLE system. **A** CAD Model (Virtual Prototype) in SolidWorks (Dimensions in mm); **B** Simscape Detailed Model; **C** Simscape Simplified Model

Table 3 Mass and Length Of The Right Leg of The PRLLE

Property	Link 1	Link 2	Link 3	Link 4	Link 5
Length (mm)	89.5	19	324	395	235
Mass (kg)	1.352	0.212	2.535	2.256	1.973

3.2 MATLAB simulink-Simscape simulation

The simulation framework was developed in MATLAB R2021a (MathWorks, USA), using the imported CAD file and employing the Simulink®, Simscape™, and Simscape Multibody™ toolboxes. Driving the dynamics of the coupled human–PRLLE system in the Simscape Detailed Model (Fig. 4B) is highly intricate. To streamline this dynamic modelling and aid in model-based controller implementation, a Simscape Simplified Model (Fig. 4C) was developed to dynamically represent the Detailed Model. Subsequently, a Simulink Model, based on the Simscape Simplified Model, was established to represent the coupled human–PRLLE system, leveraging MATLAB coding capabilities within MATLAB Function Blocks in the Simulink. Figure 5 illustrates the interaction architecture among SolidWorks™, Simscape™, and Simulink®, showcasing the interconnections between the Virtual Prototype, Detailed Model, Simplified Model, and Simulink Model. As Fig. 5 shows, the outcomes of the Simulink Model have been compared with those of the Detailed Model to validate the accuracy of the derived dynamic model.

Using the Simscape Multibody™ toolboxes, the equations of motion were formulated for the coupled human–PRLLE system, both for the Detailed and Simplified Models. Within the Simulink model, MATLAB functions were employed to script the inertia matrix (7), Coriolis and centripetal matrix (8), and gravity vector (9) for each leg. The forward dynamic problem (10) was then solved under a CTC

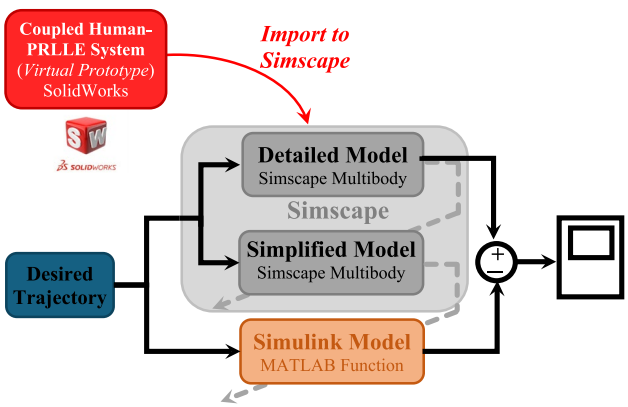

Fig. 5 Schematic representation clarifying the interrelationships among the Virtual Model, Detailed Model, Simplified Model, and Simulink Model within the simulation section

controller (11) for each model and leg using MATLAB's *ode4* (*Runge–Kutta*) solver with a fixed-step size of 0.01 s. In this study, the reported positions were digitized and filtered through a second-order, no-lag, low-pass Butterworth filter with a 1.5 Hz cutoff frequency.

An *Inertia Sensor* from the Simscape Multibody™ toolbox was employed to measure the inertia properties of each link. These properties include mass (m_i), center of mass (ℓ_{ci}), and inertia (I_i), encompassing both the moment of inertia and the product of inertia. The length of each link (a_i) is presented in Table 3, where the index i denotes the link number. For this purpose, the *Inertia Sensor* was configured using the Custom Measurement Frame, with the options for "Span Weld Joints", "Mass", "Center of Mass", and "Centered Inertia Matrix" activated. The Sensor port (S) is connected to the body group of each link in the Detailed Model, while the Measurement port (M) is attached to the corresponding link in the Simplified Model. Table 4 displays the numerical values of the inertia properties of each link of the right leg in the Simplified Model, where each link corresponds to a body group of the associated link in the Detailed Model. The numerical values in this table, pertaining to the right leg of the Simplified Model, were used to develop the Simulink Model of the right leg, while the left leg followed a similar process.

Developing the Simulink Model results in access to the inertia matrix ($M(q)$), the Coriolis and centripetal matrix $C(q, q)$, and the gravity vector ($G(q)$) for each leg independently. By comparing the Detailed Model with the Simulink Model in the subsequent section, the derived dynamic model's high accuracy will be evident, aligning with the assumptions in Sect. 2.3: $\widetilde{M}(q) = M(q)$, $\widetilde{C}(q, \dot{q}) = C(q, \dot{q})$, and $\widetilde{G}(q) = G(q)$. To configure the controller as per Eq. (11), it is sufficient to determine K_p and K_d based on Eq. (15). The proportional gain matrix (K_p) is a 5×5 diagonal matrix with each entry set to 25. Similarly, the derivative gain matrix (K_d) is a 5×5 diagonal matrix with entries set to 10, ensuring a smooth response as outlined in Eq. (15). The CTC controller is designed based on the Simulink Model and it is applied to the Detailed Model, enabling the coupled human–PRLLE system with passive human user to follow the desired joint angle trajectory input with an appropriate control signal. The designed CTC controller, combined with PID controllers, delivers assistive torque for the coupled human–PRLLE system with an active human user.

Table 4 Inertia Properties Of The Right Leg In The Simscape Simplified Model OF The Coupled Human–PRLLE System

Property	Link 1	Link 2	Link 3	Link 4	Link 5
a (mm)	89.5	19	278	361	235
m (kg)	1.352	0.212	4.525	3.102	2.194
ℓ_{cx}(mm)	12.8	3.7	− 45.6	− 62.9	− 61.3
ℓ_{cy}(mm)	− 30.2	49.4	0.15	0.04	− 17.1
ℓ_{cz}(mm)	89.9	− 0.8	− 21.3	− 2.4	0.06
I_{xx}(gm^2)	6.2	0.35	21.31	12.14	10.98
I_{yy}(gm^2)	4.62	0.13	51.37	36.48	13.41
I_{zz}(gm^2)	7.75	0.47	36.02	27.78	6.29
I_{xy}(gm^2)	0.4	0.012	− 0.05	− 0.09	− 2.6
I_{xz}(gm^2)	2.49	− 0.002	12.62	7.31	2.64
I_{yz}(gm^2)	− 0.81	− 0.09	− 0.135	− 0.17	0.92

a length, m mass, ℓ_{cj} center of mass along the j-axis, I_{kk} principal moment of inertia about the k-axis, I_{mn} product of inertia with respect to the mn-plane

4 Results and discussion

Simulation results for passive and active human user scenarios are presented. In the passive human user scenario, the PRLLE provides all required torques, whereas in the active user scenario, the PRLLE supplies only a portion, with the remainder compensated by the active user. Each simulation run took approximately 12 min on a standard desktop with an Intel Core i7 3.2 GHz CPU and NVIDIA GeForce GT 730 GPU.

4.1 Passive human user scenario

Simulations for the Detailed Model, Simplified Model, and Simulink Model were executed within a unified environment to ensure consistent simulation conditions. In this scenario, the human user remains entirely passive, with the PRLLE providing full assistance. To validate the accuracy of the derived dynamic model under the model-based CTC controller, the results for each actuated joint were compared with their respective desired trajectories. Due to the prescribed desired trajectory, it is assumed that the hip transverse joint remains fixed; consequently, results for this joint are omitted for conciseness. To validate the derived dynamic model and assess the robustness of the designed controller, simulation results were obtained under a disturbance in this scenario.

Simulation results, depicted in Fig. 6, span 30 s with each gait cycle lasting 10 s. To verify the robustness of the controlled model, a disturbance signal in the form of white noise was added to the right leg of both the Simscape and Simulink Models between 15 and 20 s, allowing comparison with the undisturbed left leg. Figure 6A panels depict the joint trajectory tracking of all actuated joints during walking, comparing the Simscape Detailed Model to the Simulink Model in the desired trajectory tracking. The initial conditions of the PRLLE joint angles are zero, markedly differing from those of the desired trajectories. The PRLLE joint

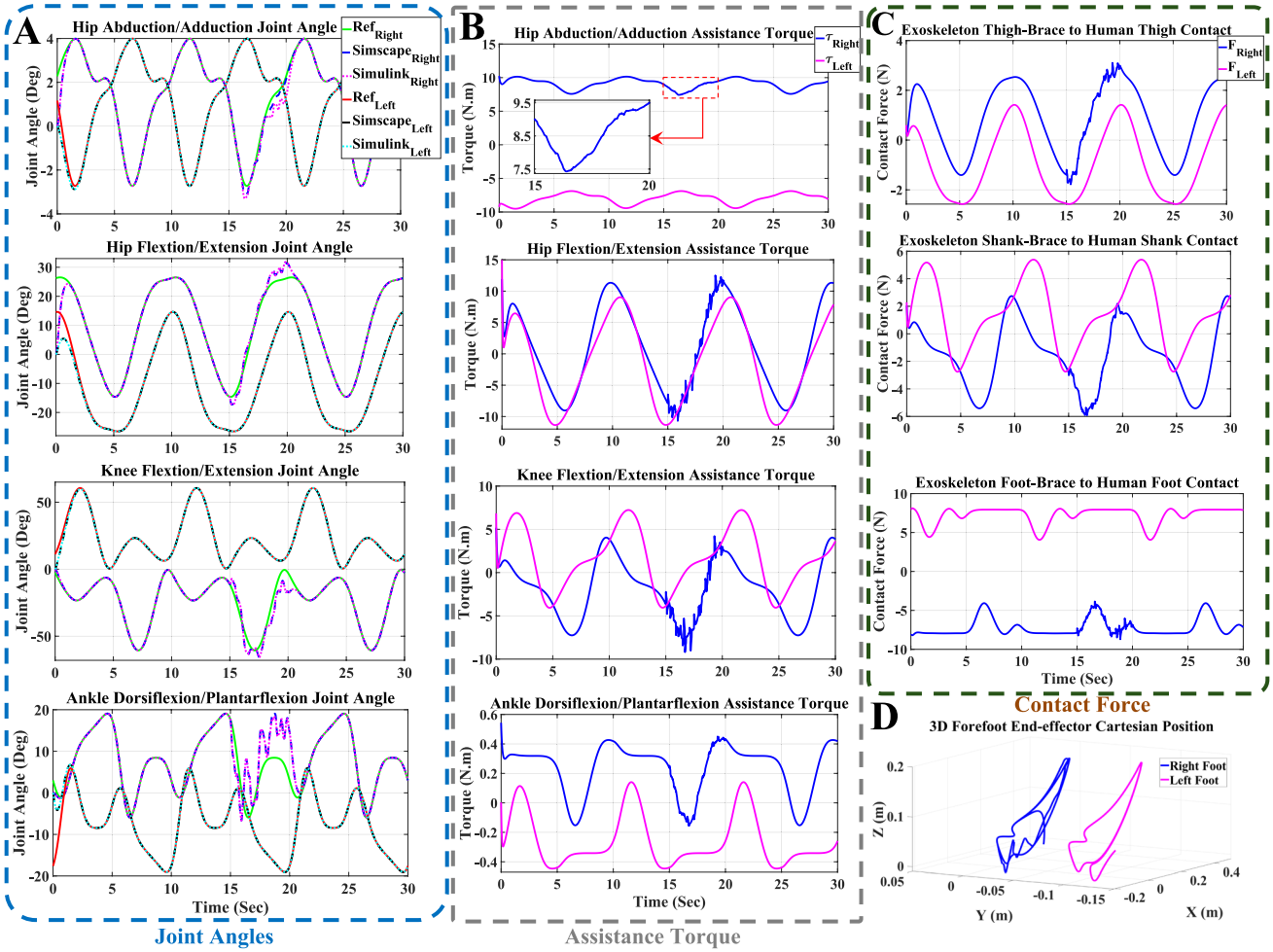

Fig. 6 Simulation of the PRLLE's right and left legs during a 30-s walk with Passive Human User: **A** Joint Angles; **B** Assistance Torques; **C** Contact Forces (Note: Displayed results exclusively pertain to forces exerted perpendicularly to the segment length); **D** Three-Dimensional (3D) Trajectory of Forefoot End-Effectors. Important: A disturbance affects the right leg between 15 and 20 s

angles smoothly converge and accurately track the desired trajectories under the designed control signals. Both Simscape and Simulink Models exhibit consistent trajectories, validating the accuracy of the derived dynamic model for the right and left legs. Despite the white noise disturbance to the right leg between 15 and 20 s, both the Simscape and Simulink Models maintain similar trajectories, except for the hip abduction/adduction joint. This joint is distinct from others in the PRLLE, as it is not welded to the corresponding human segment, unlike the others, resulting in a divergence in the Simscape and Simulink dynamics during the disturbance. Owing to the effectiveness of the CTC controller, joint angles converge to the desired trajectories shortly after the disturbance, underscoring the controller's robustness.

Table 5 presents the root mean square (RMS) error between the joint angles of the Simscape-Simulink Models and the desired trajectories for each leg. The primary source of the RMS error stems from the disparity in initial conditions between the models and the desired trajectories. Once the models converge to the desired trajectory, their error diminishes to a range around 10^{-7} degrees, reflecting the high accuracy of the models. As the right leg is subject to disturbance, it manifests a higher RMS error relative to the

Table 5 RMS Error Between Simscape-Simulink Models and Desired Trajectory for Each Leg

Leg	Model	Hip (A/A) (Degree)	Hip (F/E) (Degree)	Knee (F/E) (Degree)	Ankle (D/P) (Degree)
Right	Simscape	0.2400	2.6856	3.5889	3.1994
	Simulink	0.3005	2.6881	3.5979	3.2786
Left	Simscape	0.1292	1.7735	1.4396	1.6432
	Simulink	0.1292	1.7735	1.4396	1.6432

A/A Abduction/Adduction, *F/E* Flexion/Extension, *D/P* Dorsiflexion/Plantarflexion. Note: The right leg was affected by a disturbance between 15 and 20 s

desired trajectory than the undisturbed left leg, as evidenced in the table. While the Simscape and Simulink Models display similar RMS errors for the undisturbed left leg, the Simscape Model provides superior tracking of the desired trajectory for the disturbed right leg compared to the Simulink Model. Despite the controller being designed for the Simulink Model and subsequently applied to the Simscape Model, the latter demonstrates superior tracking results in the disturbed right leg compared to the Simulink Model.

Since the dynamic model of the coupled human–PRLLE system in the Simulink Model is derived at low frequencies, it fails to capture the system's dynamic behavior at the high frequencies present in the white noise disturbance. The high-frequency white noise disturbance in the Simscape Model actively triggers interaction forces between the PRLLE and the human (as shown in Fig. 6C), dynamics not fully included by the Simulink Model at high frequencies. This issue is exacerbated for the hip abduction/adduction joint, where no interaction force exists between the PRLLE and the human user. Figure 6A and Table 5 demonstrate that the disturbance significantly affects the coupled human–PRLLE segments connected via contact joints compared to uncoupled segments. This observation indicates that the human–PRLLE interaction force is highly susceptible to disturbances, while the uncoupled segment demonstrates greater robustness against such disturbances. Furthermore, Fig. 6A reveals that the left leg lags a half-gait phase behind the right leg. Both the right and left legs demonstrate the same rotation direction in the hip abduction/adduction joints located in the frontal plane. Conversely, other joints situated in the sagittal plane rotate in opposite directions.

The panels in Fig. 6B illustrate the assistance torques for joints in both the right and left legs associated with the Simscape Detailed Model. These diagrams indicate that as the actuator carries additional segments, the applied torque increases correspondingly. Notably, the ankle joint, which solely supports the ankle, exerts minimal torque, while the hip joint—bearing the entire leg's weight—exerts maximum torque. Furthermore, all PRLLE joint torques are observed to oscillate around zero, intermittently reaching zero Newton-meters (Nm), except for the hip abduction/adduction joints in the frontal plane. The torque for the joints in the frontal plane does not reach zero; instead, it averages approximately + 10 Nm for the right leg and – 10 Nm for the left leg. This anomaly occurs because this scenario does not account for interaction between the human–PRLLE system and the ground. Without ground reaction forces, the equilibrium points for the frontal joint angles are – 45° for the right leg and 225 for the left leg, with the sagittal joint angles stabilizing at 0°. The desired joint trajectories for sagittal joints encompass the equilibrium point, whereas those for frontal plane joints significantly deviate from their respective equilibrium points, never including them. When joints attain their equilibrium point, their torque reaches zero. Consequently, sagittal joints are anticipated to achieve zero Nm, while frontal joints will not, as observable in Fig. 6B. Additionally, Fig. 6B displays the disturbance in the right leg caused by white noise in this scenario. The noise, introduced directly to the joint torque signals of the right leg, is evident between 15 and 20 s.

The panels in Fig. 6C show the interaction forces between the PRLLE and the human user across the thigh, shank, and foot segments. For clarity, only forces acting perpendicular to each segment's longitudinal axis (i.e., into the limb) are reported. Although the foot segment is lighter than both the shank and thigh segments, it generates the largest interaction force through its brace between the human and the PRLLE, compared to the other segments. Moreover, it consistently maintains a nonzero average value, unlike the others. This issue originates from Table 2, where the ankle angle (θ_5) undergoes adjustments of + 90° and – 90° for the right and left feet, respectively. These adjustments cause each foot to deviate significantly from its equilibrium point. With desired angles diverging substantially from the equilibrium without convergence, a negative interaction force is anticipated for the right foot, while a positive one is expected for the left, as depicted in Fig. 6C. Additionally, due to the knee joint experiencing greater rotation than the hip joint, higher interaction forces are expected at the shank compared to the thigh, as evidenced in Fig. 6C. Finally, Fig. 6D presents the Three-Dimensional (3D) Trajectory of Forefoot End-Effectors for the disturbed right foot and undisturbed left foot, showcasing both step length and step height.

A supplementary video accompanying this paper offers enhanced understanding and visual insight into the PRLLE's motion following the provided gait pattern.

4.2 Active human user scenario

In this scenario, the PRLLE provides a portion of the required torques, with the remaining supplied by the active human user to follow a prescribed gait trajectory. The level of assistance from the PRLLE in simulations was regulated using the parameter C (Sect. 2.3.2). Results are presented for two values of C (0.3 and 0.6), comparing the consequent reduction in human torques due to PRLLE assistance. Results are presented for the right leg only, with the left leg showing mirrored outcomes with a half-gait phase shift. Figure 7A illustrates that increased torque assistance from the PRLLE results in reduced torque application by the human user in all joints during walking. Table 6 displays RMS values of torque reduction across four human joints for two levels of assist in relative to the zero assist, while Table 7 details the corresponding maximum reduction percentages.

Figure 7B depicts the required PRLLE torques in simulations at 30% and 60% assistance levels. The 60% assist

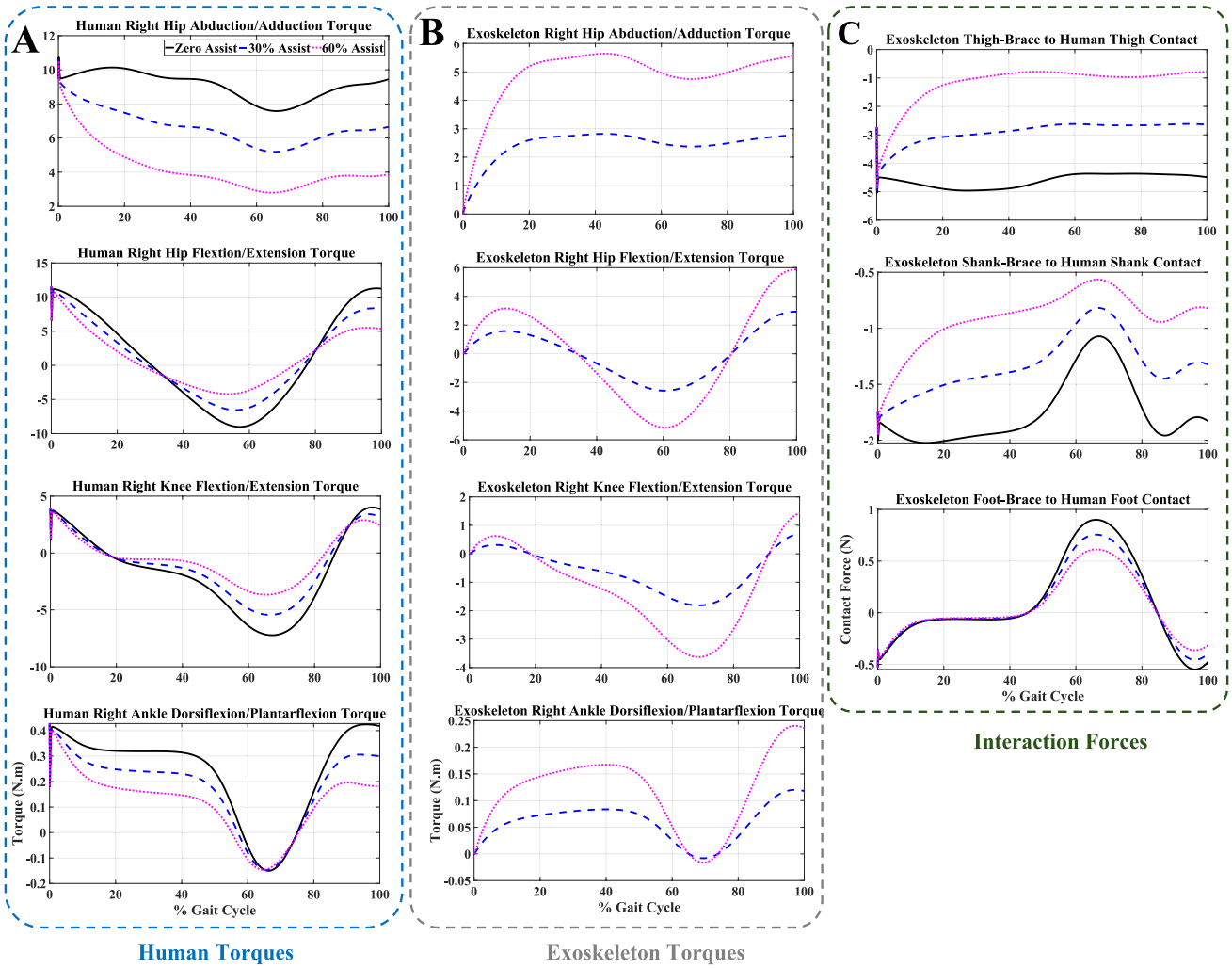

Fig. 7 Simulation results for 0%, 30%, and 60% exoskeleton torque assist with the active human (Nominal Model) over one gait cycle. **A** Panels display human joint torques at the hip (A/A), hip (F/E), knee (F/E), and ankle (P/D) joints, respectively; **B** Panels show exoskeleton actuator torques at the hip (A/A), hip (F/E), knee (F/E), and ankle (P/D) joints, respectively; **C** Interaction forces between the human model and the PRLLE at different assistance levels, illustrated at the Thigh-brace, Shank-brace, and Foot-brace; Force signals are presented exclusively for forces exerted perpendicular to the segment length

Table 6 RMS Reduction in Torques of the Nominal Human Model with 30% and 60% PRLLE Assistance

Rate of assistance	Hip (A/A)	Hip (F/E)	Knee (F/E)	Ankle (P/D)
30% Assist	2.4970	1.6466	0.9544	0.0686
60% Assist	4.9939	3.2931	1.9088	0.1371

Table 7 Percentage of Maximum Torque Reduction in the Nominal Human Model with 30% and 60% PRLLE Assistance

Rate of assistance	Hip (A/A)	Hip (F/E)	Knee (F/E)	Ankle (P/D)
30% Assist	26.3%	25.4%	25.1%	28.0%
60% Assist	52.6%	50.8%	50.3%	56.2%

Table 8 Peak Power Requirements of PRLLE Actuators During Walking

Rate of assistance	Hip (A/A)	Hip (F/E)	Knee (F/E)	Ankle (P/D)
30% Assist	9.0 W	39.7 W	49.2 W	1.2 W
60% Assist	18.1 W	79.5 W	98.5 W	2.4 W

PRLLE exhibited higher torques compared to the 30% assist, as anticipated. However, it is crucial to mention that the torques exerted by the PRLLE do not necessarily equal the human joint torque reduction. This discrepancy is attributed to the misalignment of PRLLE actuators, particularly the frontal hip actuator, with the human model's joints during motion. Furthermore, Table 8 details the maximum power

requirements calculated for each PRLLE actuator. Consistent findings were noted for both the 8-year-old female and 12-year-old male models, showing a decrease in human hip, knee, and ankle joint torques with escalating PRLLE assist levels (Results omitted for brevity and to enhance paper readability).

As mentioned earlier, the PRLLE interacts with the human model by transmitting forces and torques at contact points, which are modeled as weld joints (see Sect. 3.1). The interaction forces between the PRLLE and the nominal human model are depicted in Fig. 7C panels. For clarity, the report focuses solely on forces acting perpendicular to the longitudinal axis of each segment, i.e., forces directed into the limb. The observation reveals that the largest interaction forces for the prescribed gait trajectory occur at the Thigh attachment, with the next highest at the Shank attachment. Figure 7C panels show that a decrease in assist levels leads to an increase in interaction forces. Moreover, variations in contact forces were anticipated for the 8-year-old female and 12-year-old male models, owing to dynamic differences. Table 9 details the relative change in maximum contact force for both model variants and PRLLE assists, relative to the nominal model's corresponding values. Findings show higher contact forces for the 12-year-old male model and lower for the 8-year-old female model.

4.3 Comparison with state-of-the-art technologies

Current literature on pediatric exoskeletons is limited, particularly for devices with multiple DOFs designed for children aged 8–12 years. Most existing systems focus on single-joint designs or lack detailed dynamic modeling for human–robot interaction (Sarajchi et al. 2021). In contrast, the proposed PRLLE offers a novel design with five actuated joints per leg, enabling dynamic simulations for both passive and active users. The CTC strategy used in this study achieves significant torque reductions (up to 56%), surpassing results reported for similar adult-focused systems (Sarajchi et al. 2021). Additionally, the power requirements of the actuators, peaking at 98W, align with benchmarks in wearable robotics, ensuring practicality.

The results of this simulation-based study indicate that PRLLEs have the potential for practical implementation, with robust control strategies and manageable power requirements. However, real-world applications involve unique challenges, including physiological variability among users, ensuring user comfort, and guaranteeing device safety. As a preliminary validation strategy, we propose testing the PRLLE on static or dynamic frames and using child-sized dummies to refine the control mechanisms and evaluate interaction forces. This staged approach minimizes risks while facilitating the transition from simulation to experimental testing.

5 Conclusion

This study analyzed human–PRLLE interaction during walking, examining passive and active users with varied PRLLE torque assistance across different ages. It meticulously developed a dynamic model and a model-based controller for a unique PRLLE, designed with adjustable sizing to accommodate children aged 8 to 12 based on an anthropometric data. The PRLLE, featuring five DOFs per leg, possesses actuated frontal hip, sagittal hip, knee, and ankle joints in simulations while maintaining a passive hip transverse joint. A virtual prototype of a coupled human–PRLLE system, designed in SolidWorks™, is imported into Simscape™ as "Detailed Model." Following multiple layers of simplification applied to the "Detailed Model" using the Simscape Multibody™ toolbox, a "Simplified Model" is developed. This model facilitates the derivation of the dynamic model through the Euler–Lagrange formulation, employing forward kinematic analysis based on the Denavit–Hartenberg convention. The formulated dynamic model within the Simulink® environment represents each leg with a distinct MATLAB Function.

This study presented two distinct controller frameworks: one designed for passive human interaction, and another designed for active human engagement. In the former controller framework, an independent model-based CTC controller is designed for each leg, enabling precise trajectory tracking with minimal discrepancies. The validation process of the derived dynamic model, under the designed CTC controller, involves comparing outputs from both Detailed and Simplified Models with the desired trajectories for each actuated joint. Introducing white noise disturbance to the right leg for control robustness assessment, the simulation results obtained offer conclusive validation of the derived dynamic model and underscore the effectiveness of the controller for passive human user.

Table 9 Percentage Change in Maximum Contact Forces: Comparison Between Smaller and Larger Human Models Relative to the Nominal Model

Human model	Rate of assist	Hip (A/A)	Hip (F/E)	Knee (F/E)	Ankle (P/D)
8-year-old Female	30%	102.1%	122.6%	108.5%	110.9%
	60%	102.1%	122.2%	108.6%	111.1%
12-year-old Male	30%	94.1%	79.8%	90.8%	72.4%
	60%	90.2%	80.1%	90.5%	70.5%

The latter controller framework integrates the previously described CTC controller with PID controllers to effectively control the integration between the human and PRLLE. This integration ensures adherence to a predefined gait trajectory for an active human user. Simulation results indicate that an increase in PRLLE assistance torque leads to a corresponding decrease in human contribution, thereby reducing the amplitude of human–exoskeleton interaction forces. Observations reveal that contact forces vary significantly with the PRLLE's assist level and the user's size, emphasizing the effectiveness and the need for model-based studies to virtually test various human and PRLLE configurations. This simulation-based study provides a robust foundation for experimental validation and bridges the gap between theoretical modeling and practical implementation of the PRLLE.

6 Future works

In this study, human–PRLLE interaction is analyzed only in a simulation environment. Future research will present experimental results using the dynamic model derived in this simulation study. In future work, the PRLLE will be mounted on a frame, and using the kinematic and dynamic analysis from this study, the dynamic model of the mounted PRLLE, both with and without a child-sized dummy, will be derived. After unmounting the PRLLE, a model-based controller will be designed to facilitate the user's walk with the PRLLE in two distinct modes: (i) passive user, where the user exerts no force, and (ii) active user, where the user exerts force, using the derived dynamic model from the simulation. The differential outcomes between active and passive modes will quantify the human–PRLLE interaction energy, which will be optimized with the model-based controller using Central Pattern Generators (CPGs)-based gait planning. Future experimental work will include benchmarking the PRLLE against available pediatric exoskeleton systems to further validate its performance and highlight its unique strengths.

Appendix A

The components of the inertia matrix, Coriolis and centripetal matrix, and gravity vector pertaining to the right leg of the coupled human–LLE system can be accessed at https://github.com/sarajchi/PLLE-Sim/tree/Appendix.

Appendix B

The simulation model and its results can be accessed under an open-source license at https://github.com/sarajchi/PLLE-Sim/tree/main.

Supplementary Information The online version contains supplementary material available at https://doi.org/10.1007/s41315-025-00421-x.

Acknowledgements Our sincere thanks go to our collaborative partner at JUNIA-HEI, Lille, France, for their valuable contributions to the MOTION project.

Author contributions Conceptualization, M.S. and K.S.; methodology, M.S.; hardware: M.S.; software, M.S.; validation, M.S.; formal analysis, M.S.; investigation, M.S.; resources, M.S.; data curation, M.S.; writing—original draft preparation, M.S.; writing—review and editing, M.S.; visualization, M.S.; supervision, K.S.; project administration, K.S.; funding acquisition, K.S. Both authors have read and agreed to the published version of the manuscript.

Funding The authors acknowledge receipt of the following financial support for the research, authorship, and publication of this article: Interreg 2 Seas programme 2014–2020 co-funded by the European Regional Development Fund under subsidy contract No. 2S05-038 (M.O.T.I.O.N project).

Data or code availability Data are provided in the appendices, and further information is available upon request.

Declarations

Conflict of interest The authors declare no competing interests.

Ethical approval Not applicable.

Consent to participate Not applicable.

Consent for publication Not applicable.

References

3D Human Model, "Free Demo Model SOLIDWORKS," [Online]. Available: https://3dhumanmodel.com/product/free-demo-model-solidworks-not-commercial-use/. Accessed 11 May 2021

Aisen, M.L., Kerkovich, D., Mast, J., Mulroy, S., Wren, T.A., Kay, R.M., Rethlefsen, S.A.: Cerebral palsy: clinical care and neurological rehabilitation. Lancet Neurol. **10**(9), 844–852 (2011)

Alexander, M.A., Dennis, J.M., Murphy, K.P.: Pediatric Rehabilitation: Principles and Practice, 5th edn. Demos. Medical. Pub, New York, NY, USA (2015)

Andrade, R. M., Sapienza, S., Bonato, P.: Development of a "transparent operation mode" for a lower-limb exoskeleton designed for children with cerebral palsy, in *IEEE 16th Int. Conf. Rehabil. Robot.*, Toronto, Canada (2019)

Bair, M.O.: The Design and Testing of a Powered Exoskeleton to Reduce the Metabolic Cost of Walking in Individuals with Cerebral Palsy. Northern Arizona University, Flagstaff, AZ (2018)
Baud, R., Manzoori, A.R., Ijspeert, A., Bouri, M.: Review of control strategies for lower-limb exoskeletons to assist gait. J. Neuroeng. Rehabil. **18**, 1–34 (2021)
Bjornson, K.F., Belza, B., Kartin, D., Logsdon, R., McLaughlin, J.F.: ambulatory physical activity performance in youth with cerebral palsy and youth who are developing typically. Phys. Ther. **87**(3), 248–257 (2007)
Centers for Disease Control and Prevention, "Data and Statistics for Cerebral Palsy," Centers for Disease Control and Prevention, 2 May 2022. [Online]. Available: https://www.cdc.gov/ncbddd/cp/data.html. Accessed 11 Aug 2023
Chae, S., Choi, A., Jung, H., Kim, T.H., Kim, K., Mun, J.H.: Machine learning model to estimate net joint moments during lifting task using wearable sensors: a preliminary study for design of exoskeleton control system. Appl. Sci. **11**(24), 1–14 (2021)
Chen, Z., Guo, Q., Li, T., Yan, Y.: Output constrained control of lower limb exoskeleton based on knee motion probabilistic model with finite-time extended state observer. IEEE/ASME Trans. Mechatron. **28**(4), 2305–2316 (2023)
Denavit, J., Hartenberg, R.S.: A kinematic notation for lower-pair mechanisms based on matrices. J. Appl. Mech. **22**(2), 215–221 (1955)
Duan, D., Goemans, N., Takeda, S., Mercuri, E., Aartsma-Rus, A.: Duchenne muscular dystrophy. Nat. Rev. Dis. Primers. **7**(1), 1–19 (2021)
Fryar, C. D., Gu, Q., Ogden, C. L.: Anthropometric reference data for children and adults; United States, 2007–2010. Centers for Disease Control and Prevention, Oct. 2012. [Online]. Available: https://stacks.cdc.gov/view/cdc/12223. Accessed Aug. 2023
Goo, A., Laubscher, C.A., Wiebrecht, J.J., Farris, R.J., Sawicki, J.T.: Hybrid zero dynamics control for gait guidance of a novel adjustable pediatric lower-limb exoskeleton. Bioeng. **9**(5), 1–15 (2022)
Han, S., Wang, H., Tian, Y., Christov, N.: Time-delay estimation based computed torque control with robust adaptive RBF neural network compensator for a rehabilitation exoskeleton. ISA Trans. **97**, 171–181 (2020)
Hasnain-Baluch, T., Masood, A., Iqbal, J., Izhar, U., Shahbaz-Khan, U.: Kinematic and dynamic analysis of a lower limb exoskeleton. Int. J. Mech. Mechatron. Eng. **6**(9), 1945–1949 (2012)
Hess-Coelho, T.A., Cortez, M., Moura, R.T., Forner-Cordero, A.: Progressive improvement of the model of an exoskeleton for the lower limb by applying the modular modelling methodology. Mach **10**(4), 1–16 (2022)
Hsu, W.-C., Sugiarto, T., Lin, Y.-J., Yang, F.-C., Lin, Z.-Y., Sun, C.-T., Hsu, C.-L., Chou, K.-N.: Multiple-wearable-sensor-based gait classification and analysis in patients with neurological disorders. Sensors **18**(10), 3397 (2018)
John, E.R., Prichep, L., Ahn, H., Easton, P., Fridman, J., Kaye, H.: Neurometric evaluation of cognitive dysfunctions and neurological disorders in children. Prog. Neurobiol. **21**(4), 239–290 (2003)
Layne, C.S., Malaya, C.A., Ravindran, A.S., John, I., Francisco, G.E., Contreras-Vidal, J.L.: Distinct kinematic and neuromuscular activation strategies during quiet stance and in response to postural perturbations in healthy individuals fitted with and without a lower-limb exoskeleton. Front. Hum. Neurosci. **16**, 1–12 (2022)
Lunn, M.R., Wang, C.H.: Spinal muscular atrophy. The Lancet **371**(9630), 2120–2133 (2008)
Luo, L., Jeat-Foo, M., Ramanathan, M., Kai-Er, J., Chiam, C.H., Li, L., Yau, W.Y., Ang, W.T.: Trajectory generation and control of a lower limb exoskeleton for gait assistance. J. Intell. Robot. Syst. **106**, 1–15 (2022)
Luo, S., Jiang, M., Zhang, S., Zhu, J., Yu, S., Silva, I.D., Wang, T., Rouse, E., Zhou, B., Yuk, H., Zhou, X., Su, H.: Experiment-free exoskeleton assistance via learning in simulation. Nature **630**, 353–359 (2024)
Lynch, K.M., Park, F.C.: Modern Robotics: Mechanics, Planning, and Control. Cambridge University Press, Cambridge (2017)
Manns, P., Sreenivasa, M., Millard, M., Mombaur, K.: Motion optimization and parameter identification for a human and lower back exoskeleton model. IEEE Robot. Autom. Lett. **2**(3), 1564–1570 (2017)
Mutch, L., Alberman, E., Hagberg, B., Kodama, K., Perat, M.V.: Cerebral palsy epidemiology: where are we now and where are we going? Dev. Med. Child Neurol. **34**(6), 547–551 (1992)
Orekhov, G., Fang, Y., Luque, J., Lerner, Z.F.: Ankle exoskeleton assistance can improve over-ground walking economy in individuals with cerebral palsy. IEEE Trans. Neural Syst. Rehabil. Eng. **28**(2), 461–467 (2020)
Parent, S., Mac-Thiong, J.-M., Roy-Beaudry, M., Sosa, J.F., Labelle, H.: Spinal cord injury in the pediatric population: a systematic review of the literature. J. Neurotrauma **28**(8), 1515–1524 (2011)
Rosenbaum, P., Paneth, N., Leviton, A., Goldstein, M., Bax, M.: A report: the definition and classification of cerebral palsy April 2006. Dev. Med. Child Neurol. **49**, 8–14 (2007)
Rupal, B.S., Rafique, S., Singla, A., Singla, E., Isaksson, M., Virk, G.S.: Lower-limb exoskeletons: research trends and regulatory guidelines in medical and non-medical applications. Int. J. Adv. Robot. Syst. **14**(6), 1–27 (2017)
Saeed, M.T., Gul, J.Z., Kausar, Z., Mughal, A.M., Din, Z.M., Qin, S.: Design of model-based and model-free robust control strategies for lower limb rehabilitation exoskeletons. Appl. Sci. **12**(8), 1–18 (2022)
Sarajchi, M.: Design and Control of a Paediatric Robotic Lower-Limb Exoskeleton. University of Kent, Canterbury (2024)
Sarajchi, M., Sirlantzis, K.: Design and control of a single-leg exoskeleton with gravity compensation for children with unilateral cerebral palsy. Sensors **23**(13), 1–35 (2023)
Sarajchi, M., Sirlantzis, K.: Pediatric robotic lower-limb exoskeleton: an innovative design and kinematic analysis. IEEE ACCESS **11**, 115219–115230 (2023)
Sarajchi, M., Al-Hares, M.K., Sirlantzis, K.: Wearable lower-limb exoskeleton for children with cerebral palsy: a systematic review of mechanical design, actuation type, control strategy, and clinical evaluation. IEEE Trans. Neural Syst. Rehabil. Eng. **29**, 2695–2720 (2021)
Slucock, T.: A systematic review of low-cost actuator implementations for lower-limb exoskeletons: a technical and financial perspective. J. Intell. Robot. Syst. **106**, 1–31 (2022)
Spong, M.W., Hutchinson, S., Vidyasagar, M.: Robot Modeling and Control. Wiley, New York (2006)
Swoboda, K.J.: Seize the day: Newborn screening for SMA. Am. J. Med. Genet. A **152**(7), 1605–1607 (2010)
Tucker, M.R., Olivier, J., Pagel, A., Bleuler, H., Bouri, M., Lambercy, O., Millán, J., Riener, R., Vallery, H., Gassert, R.: Control strategies for active lower extremity prosthetics and orthotics: a review. J. Neuroeng. Rehabil. **12**(1), 1–30 (2015)
Vantilt, J., Tanghe, K., Afschrift, M., Bruijnes, A.K., Junius, K., Geeroms, J., Aertbeliën, E., Groote, F.D., Lefeber, D., Jonkers, I., Schutter, J.D.: Model-based control for exoskeletons with series elastic actuators evaluated on sit-to-stand movements. J. Neuroeng. Rehabil. **16**, 1–21 (2019)
Whitley, E., Gunnell, D., Smith, G.D., Holly, J.M., Martin, R.M.: Childhood circumstances and anthropometry: the Boyd Orr cohort. Ann. Hum. Biol. **35**(5), 518–534 (2009)

World Health Organization: Neurological disorders: public health challenges. WHO, Geneva (2006)
Yan, T., Cempini, M., Oddo, C.M., Vitiello, N.: Review of assistive strategies in powered lower-limb orthoses and exoskeletons. Robot. Auton. Syst. **64**, 120–136 (2015)
Yan, L.J., Shen, Q.M., Yang, D., Qiao, J. M., Datseris, P.: Kinematic and Dynamic Modeling and Analysis of a Lower Extremity Exoskeleton, in *16th Int. Conf. Ubiquitous Robot.*, Jeju, South Korea (2019)
Yan, Y., Chen, Z., Huang, C., Chen, L., Guo, Q.: Human–exoskeleton coupling dynamics in the swing of lower limb. Appl. Math. Model. **104**, 439–454 (2024)
Yu, Z., Zhao, J., Chen, D., Chen, S., Wang, X.: Adaptive gait trajectory and event prediction of lower limb exoskeletons for various terrains using reinforcement learning. J. Intell. Robot. Syst. **109**, 1–20 (2023)

Mohammadhadi Sarajchi received a B.Sc. and M.Sc. (Hons.) in Electrical Engineering. He earned his Ph.D. in Electronic Engineering from the School of Engineering at the University of Kent, where he developed and controlled a pediatric robotic lower limb exoskeleton. He is currently a research fellow in human-robot interaction at the Bristol Robotics Laboratory, Bristol, UK, developing a smart walker for older adults and controlling an upper limb exoskeleton. His academic journey includes being a Visiting Scholar with JUNIA-HEI in 2022 and a Researcher with Royal Holloway, University of London, from 2018 to 2019. He also spent time as a Visiting Scholar with the Mechanical Engineering Department at Tsinghua University in 2017. Since 2023, he has been engaged as a Graduate Research Assistant with the School of Engineering, Technology and Design at Canterbury Christ Church University (CCCU). Additionally, he served as a Graduate Teaching Assistant with the School of Engineering at the University of Kent for four years. His research interests include robotic control, physical human–robot interaction, and exoskeletons, contributing to significant advancements in these areas. He received the IET Postgraduate Research Award in 2023.

Konstantinos Sirlantzis is currently a Professor of applied artificial intelligence with the School of Engineering, Technology and Design, Canterbury Christ Church University (CCCU), Canterbury, Kent, U.K. Previously, he was an Associate Professor of intelligent systems with the School of Engineering, University of Kent, where he was the Head of the Robotics and Assistive Technologies Research Group and the Founding Director of the Kent Assistive RObotics Laboratory (KAROL). He has a strong track record in artificial intelligence and neural networks for image analysis and understanding, and robotic systems, with an emphasis on assistive technologies and pattern recognition for biometrics-based security applications. He has authored over 130 peer-reviewed papers in journals and conferences. He has organized and chaired a range of international conferences and workshops.